Check for updates

IET Electric Power Applications

WILEY

The Institution of Engineering and Technology

ORIGINAL RESEARCH OPEN ACCESS

2-D Electromagnetic Analysis Coupled With 3-D Thermal Analysis of a Dual-PM Excited Flux-Switching Generator With Overhang Structure for Direct Drive Wind Turbines

Amir Ebrahimi Shohani[1] | Mohammad Farahzadi[2] | Salman Ali[3] | Karim Abbaszadeh[1] | Fabrizio Marignetti[3] | Fariba Farrokh[4]

[1]Faculty of Electrical Engineering, K. N. Toosi University of Technology, Tehran, Iran | [2]Faculty of Electrical Engineering, University of Science and Culture, Tehran, Iran | [3]Faculty of Electrical and Information Engineering, University of Cassino and Southern Lazio, Cassino, Italy | [4]Faculty of Electrical Engineering, Shahrood University of Technology, Shahrood, Iran

Correspondence: Amir Ebrahimi Shohani (amir_ebrahimi@email.kntu.ac.ir)

Received: 17 January 2025 | **Revised:** 14 April 2025 | **Accepted:** 24 April 2025

Handling Editor: Zhongze Wu

Funding: The authors received no specific funding for this work.

Keywords: finite element analysis | permanent magnet generators | thermal analysis | wind turbines

ABSTRACT

This study introduces a new outer-rotor dual-permanent magnet (PM) excited flux-switching generator with an overhang structure for direct-drive wind turbine applications. The proposed generator incorporates flux barriers and ferrite PMs in the stator while utilising neodymium PMs in the rotor segments. Contrary to ferrite PMs, neodymium PMs are prone to demagnetisation in high-temperature conditions. Given that the operating temperature of the stator is nearly double that of the rotor in this study, ferrite PMs are strategically positioned in the stator to mitigate this issue. The main goal of this paper is to provide a fast and accurate method to study the electromagnetic-thermal performance of the generator. Hence, a two-dimensional finite element analysis (2-D FEA) electromagnetic analysis is coupled with a 3-D FEA thermal analysis. Moreover, a precise thermal circuit of each generator's element is displayed. Finally, the accuracy of the method is confirmed through a comparison of the simulation results with experimental data, indicating a small margin of error.

1 | Introduction

Green energy production has become more and more popular in the last decades since the majority of electricity production relies on fossil fuels, leading to more greenhouse gases, carbon emissions and a climate change crisis [1, 2]. Also, the cost of fossil fuels and possible shortages are other reasons for international communities to consider renewable energies [3]. Among all the green energy technologies, wind power generation has received considerable attention due to its accessibility, low maintenance requirements and commercial prospects [4]. It is noteworthy that the theoretical maximum efficiency of a wind turbine is 59.3% according to the Betz–Joukowsky limit [5] due to aerodynamic losses. Hence, to increase efficiency, direct drive systems are preferable to gear drive systems. Eliminating mechanical transmission elements such as chains, belts or gearboxes leads to higher system efficiency, less mechanical maintenance, less heat production and more area capacity [6, 7]. For direct drive applications, flux-switching permanent-magnet (FSPM) machines are suitable candidate owing to their high power/torque density and efficiency [8, 9]. FSPM machine was first introduced as a single-phase generator in 1955 [10]. The rated speed and power for this generator were 50,000 rpm and 3 kW, respectively. Also, a three-phase FSPM machine was first

This is an open access article under the terms of the Creative Commons Attribution License, which permits use, distribution and reproduction in any medium, provided the original work is properly cited.

© 2025 The Author(s). *IET Electric Power Applications* published by John Wiley & Sons Ltd on behalf of The Institution of Engineering and Technology.

mentioned in 1997 [11]. In conventional FSPM machines, the armature windings and PMs are installed in the stator, resulting in a simple and robust rotor structure. This topology has its pros and cons. One advantage is that this machine is an appropriate candidate for high-speed applications thanks to its simple rotor structure. Also, the conventional FSPM machine has a high air gap flux density due to the stator structure. However, the machine's doubly salient nature leads to high cogging torque, which has always challenged the designers.

Furthermore, the thermal management and demagnetisation of PMs as a result of heat generation in the stator is another concern for them. In ref. [12], an inner-rotor FSPM machine with an aerofoil-shaped rotor has been investigated. This machine included radial housing inlets to maximise self-cooling. 3-D finite element analysis (FEA) was employed to validate electromagnetic performance, while the computational fluid dynamics (CFD) model of the machine was utilised for thermal analysis. Although these methods have high accuracy and low error, they are also quite time-consuming. Moreover, the CFD method requires a supercomputer, which is not available in most research labs. In refs. [13, 14], the lumped-parameter thermal network (LPTN) model of the proposed FSPM machines has been presented to measure the temperature of different components. In ref. [13], an outer-rotor FSPM machine under driving cycles was studied, whereas in ref. [14], a double-rotor structure was investigated. Nevertheless, the LPTN method is fast, the accuracy is not precise and the margin of error is significant [15]. In refs. [16, 17], both LPTN and CFD methods were utilised to evaluate the thermal behaviour of FSPM machines. In ref. [17], the LPTN model of the machine is only constructed in the radial direction, while the axial direction has been ignored, which results in a higher margin of error in calculations. A segmented PM consequent pole flux switching machine has been developed In ref. [18]. The stator incorporates several cooling channels (ducts) to prevent PM demagnetisation and enhance heat dissipation. A 3-D model of the proposed machine has been used based on finite element analysis, to assess the electromagnetic performance and temperature distribution. However, it is worth noting that this method is considered time-consuming. Moreover, the hottest spot of the machine has occurred in the coils, which is 46°C, and this value is unreasonably low for an air-cooled machine. A bidirectional coupling model of an inner-rotor FSPM machine was investigated in ref. [19]. 2-D FEA and a 3-D asymmetric minimum element of the discussed machine have been established to reduce the computation time. However, the research only covered the machine's performance in a cold state, with no information available about its performance in a hot state. Additionally, the 3-D temperature distribution model of each component has not been analysed separately. In ref. [20], the LPTN method of the generator was discussed. However, this method requires extensive manual calculations, resulting in a significant margin of error. In contrast, this study does not face such issues. Moreover, ref. [21] presents a 3-D FEA model of the generator. While employing a 3-D FEA model for electromagnetic analysis results in substantial computational time, this paper proposes the use of a 2-D FEA model to address this issue effectively and to investigate other aspects and features of the proposed generator. This methodology not only ensures adequate accuracy but also significantly reduces computational time. Based on a thorough review of previous studies, this research aims to conduct a comprehensive analysis of electromagnetic and thermal behaviour in a new outer-rotor dual-PM flux-switching generator. For electromagnetic performance, a 2-D model, and for thermal analysis, a 3-D model of the proposed machine will be used through finite element analysis. This method can be considered a fast and accurate technique due to the comparative results between the simulation and experimental data, which will be discussed later. Moreover, to improve the accuracy of the thermal behaviour, the electromagnetic and thermal performance will be analysed in two stages. First, the resistance of the winding and the properties of the PMs will be calculated in the cold state (ambient temperature), and the generator's behaviour will be analysed based on the cold state data. Then, in the next stage, the generator's electromagnetic and thermal performance will be examined based on the winding's resistance and PMs' properties in the hot state (operating conditions). Unlike ferrite PMs, neodymium magnets are susceptible to demagnetisation in high-temperature conditions. Therefore, the proposed generator utilises ferrite magnets in the stator yoke and neodymium magnets in the rotor segments, as the rotor operates at lower temperatures. Hence, this generator is known as a dual-PM excited flux switching generator (DEFSG). Additionally, the stator benefits from several barriers to enhance heat dissipation. Furthermore, an overhang rotor is implemented to minimise cogging torque. Thanks to this design, this generator can operate under high-temperature conditions and provides high power density. In the following section, the generator structure is expressed, encompassing the machine topology, wind turbine characteristics, and analytical design.

Furthermore, the 2-D electromagnetic performance is evaluated in Section 3. The initial part outlines the no-load specifications, while the subsequent part presents the full-load characteristics for loss calculation. Section 4 analyses the steady-state and transient thermal behaviour of the proposed generator, whereas Section 5 compares the basic topology with the proposed topology. Also, Section 6 examines the prototyped generator's performance and reports the results. Finally, the findings of the study are concluded in Section 7.

2 | DEFSG Structure and Design

Figure 1 illustrates the 3-D model of the components of the proposed generator including the moving and stationary shaft, front and rear cap, front and rear bearing, stator and rotor. It is

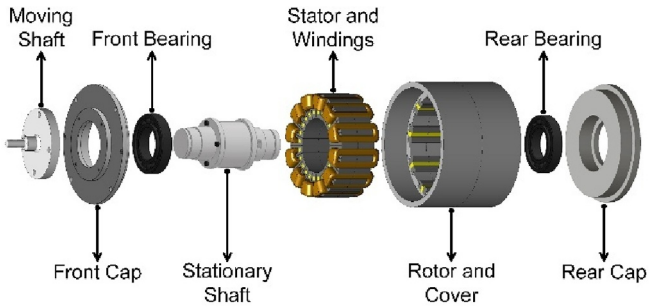

FIGURE 1 | 3-D model of each element of the DEFSG.

17518679, 2025, 1, Downloaded from https://ietresearch.onlinelibrary.wiley.com/doi/10.1049/elp2.70042 by Fabrizio Marignetti - Cochraneltalia , Wiley Online Library on [23/01/2026]. See the Terms and Conditions (https://onlinelibrary.wiley.com/terms-and-conditions) on Wiley Online Library for rules of use; OA articles are governed by the applicable Creative Commons License

noteworthy that shafts, caps, and bearings are nonmodelled elements in this study. Moreover, the procedural sequence of this study is shown in Figure 2. It can be seen that the process analysis includes two parts: 2-D electromagnetic analysis and 3-D thermal analysis.

Thermal analysis can also be divided into two categories: steady-state and transient analysis. However, the electromagnetic and steady-state thermal analysis will be repeated to adjust the winding resistance and properties of PMs.

2.1 | Machine Topology

A 2-D cross-section view of a new outer-rotor DEFSG is shown in Figure 3. Since the temperature of the stator is higher than the rotor, ferrite PMs have been chosen to be installed inside the stator yoke due to their low demagnetisation in high-temperature conditions, while neodymium PMs are sandwiched between rotor segments to increase the torque density of the proposed machine.

As can be seen, the ferrite and neodymium PMs are magnetised clockwise and anticlockwise, respectively. Moreover, the stator is equipped with a three-phase concentrated winding and various flux barriers to have better heat management. Different components of the prototyped DEFSG are shown in Figure 4. The stator core and the rotor segments are made of laminated silicon steel M600, while the stationary shaft is constructed from stainless steel 316. The stator yoke houses AC-8 ferrite PMs, and NdFeB 35 PMs are attached to the rotor segments.

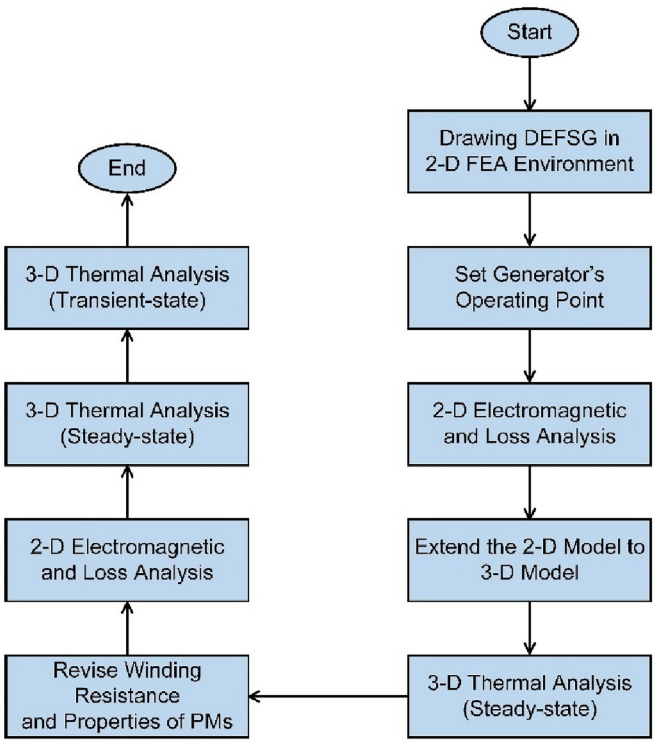

FIGURE 2 | Analysis flowchart of the proposed generator.

2.2 | Wind Turbine Characteristics

Wind turbines can be categorised into two groups based on their axis of rotation: vertical-axis wind turbines (VAWT) and horizontal-axis wind turbines (HAWT). Although VAWT is known for its higher efficiency, this study focuses on HAWT due to its self-starting capability [22]. Moreover, the output power of the wind turbine can be calculated as follows [23]:

$$P = \frac{1}{2}\rho\pi r^2 U^3 C_P(\lambda, \beta) \tag{1}$$

where ρ is the air density $\left(\mathrm{kg}/\mathrm{m}^3\right)$, r is the blade's radius (m), U is the wind speed (m/s), and $C_P(\lambda, \beta)$ is the power coefficient which can be determined by the tip speed ratio (λ) and the blade pitch angle (β). Hence, the tip speed ratio can be presented as follows [24]:

$$\lambda = \frac{\omega_r r}{U} \tag{2}$$

where ω_r is the turbine's angular velocity (rad/s). Furthermore, the wind turbine power coefficient curve is depicted in Figure 5. It is noteworthy that the blade pitch angle for this curve is zero. Before proceeding with the generator design, a study was conducted to select a realistic rated speed and power. Figure 6 shows the operating points of various commercial or reported direct-drive wind turbines taken from [25]. Based on the distribution of these points, 750 rpm and 2.3 kW were selected as the operating point for the proposed design.

2.3 | Analytical Design

The first step in the design process of an electric machine is obtaining and extracting its fundamental equations based on valid sources. FSPM machines are not excluded from this rule. Rotor pole pair number plays an important role in this type of machine. The electrical frequency of FSPM machines can be defined as follows [26]:

$$f_e = N_r f_m \tag{3}$$

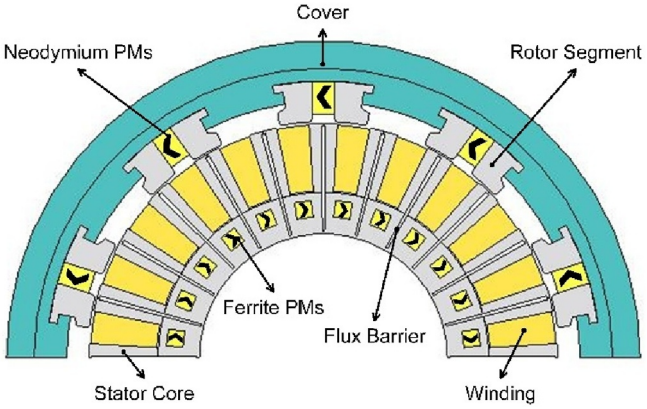

FIGURE 3 | 2-D cross-section of the DEFSG.

17518679, 2025, 1, Downloaded from https://ietresearch.onlinelibrary.wiley.com/doi/10.1049/elp2.70042 by Fabrizio Marignetti - Cochraneltalia , Wiley Online Library on [23/01/2026]. See the Terms and Conditions (https://onlinelibrary.wiley.com/terms-and-conditions) on Wiley Online Library for rules of use; OA articles are governed by the applicable Creative Commons License

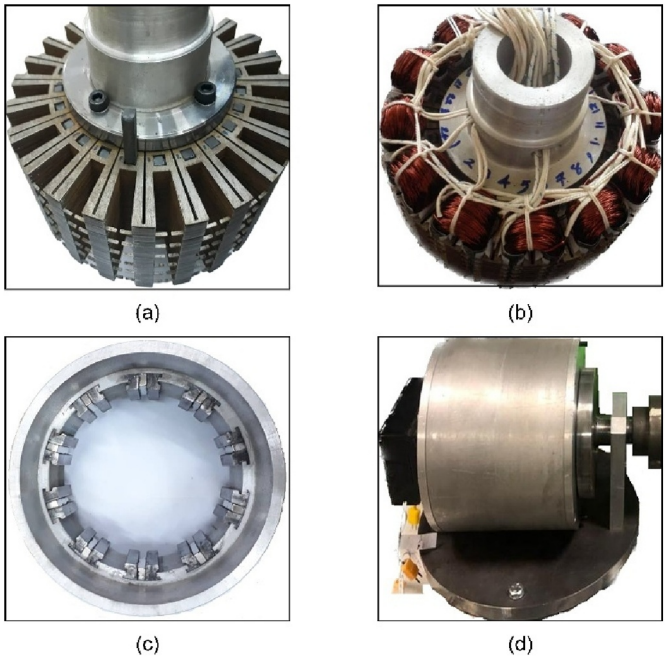

FIGURE 4 | Different elements of the prototyped generator (a) stator core and ferrite PMs, (b) stationary elements, (c) rotating elements and (d) assembled generator.

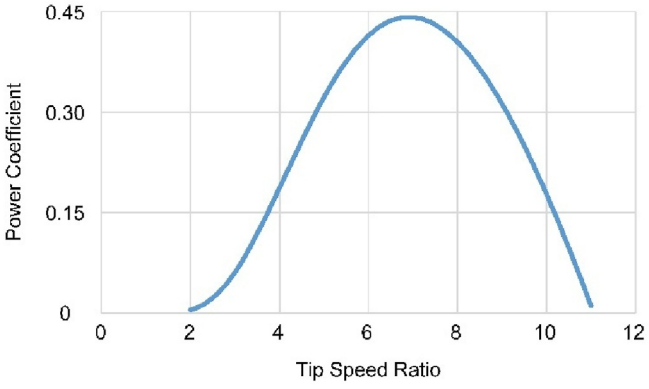

FIGURE 5 | Wind turbine power coefficient curve.

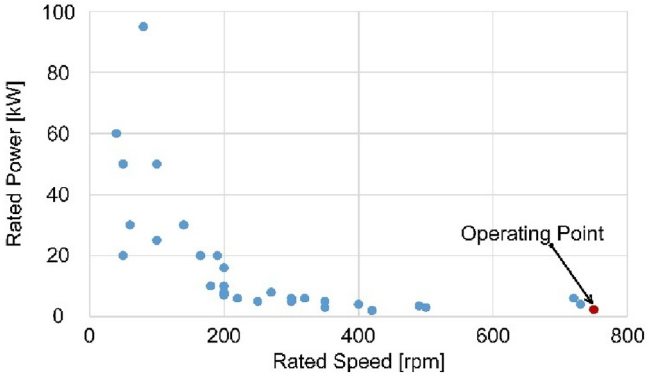

FIGURE 6 | Operating points of direct-drive wind turbines.

where f_e and f_m are the electrical and mechanical frequencies and N_r is the rotor pole pair number. Additionally, the stator pole number can be determined as follows:

$$N_s = 2(N_r \pm i) \tag{4}$$

where N_s is the stator pole number and i is a positive integer. Moreover, the output generator's power can be calculated as follows:

$$P_G = \frac{m}{2} E_m I_m \cos\varphi \tag{5}$$

where m, E_m and I_m are the phase number, the amplitude of the induced voltage and the current, respectively, and $\cos\varphi$ is the power factor. According to Faraday's law of induction, the induced voltage can be written as follows:

$$e = -n_{ph}\omega_r \frac{d\phi}{d\theta} \tag{6}$$

where n_{ph} and ω_r are the number of turns per phase and the angular speed of the rotor (rad/s). Also, ϕ is the flux linkage that passes through the coils. Hence, the induced voltage can be rewritten as follows [27]:

$$e = n_{ph}\omega_r N_r \phi_{\max} \sin(N_r\theta) = E_m \sin(N_r\theta) \tag{7}$$

As a result:

$$E_m = n_{ph}\omega_r N_r \phi_m \tag{8}$$

where:

$$\phi_m = B_{g\,\max} \frac{\pi D_{so} L}{N_s} k_d C_s \tag{9}$$

where $B_{g\,\max}$, D_{so}, L, k_d and C_s are the peak flux density (T), stator outer diameter (m), machine's active length (m), leakage

17518679, 2025, 1, Downloaded from https://ietresearch.onlinelibrary.wiley.com/doi/10.1049/elp2.70042 by Fabrizio Marignetti - Cochraneitalia , Wiley Online Library on [23/01/2026]. See the Terms and Conditions (https://onlinelibrary.wiley.com/terms-and-conditions) on Wiley Online Library for rules of use; OA articles are governed by the applicable Creative Commons License

factor and rotor pole arc coefficient, respectively. So, the maximum value of the induced voltage can be expressed as follows:

$$E_m = n_{ph} N_r B_{g\,\max} \frac{\pi D_{so} L}{N_s} k_d C_s \omega_r \tag{10}$$

Moreover, the peak current I_m can be defined as follows:

$$I_m = \sqrt{2}\,\frac{A_s \pi D_{so}}{2 m n_{ph}} \tag{11}$$

where A_s is the specific electric loading (A/m) of the machine. Finally, by substituting Equations (10) and (11) into Equation (5), the output power can be determined as given below:

$$P_G = \frac{\sqrt{2}\pi^3}{120} \frac{N_r}{N_s} D_{so}^2 L A_s B_{g\,\max} k_d C_s n \cos\varphi \tag{12}$$

where n is the speed of the rotor (rpm). Furthermore, the rotor pole arc coefficient can be presented as follows:

$$C = \frac{\text{pole\_arc}}{\text{pole\_pitch}} \approx \frac{w_{tr} N_r}{\pi} \tag{13}$$

where w_{tr} is the rotor tooth angle. The parameter characteristics of DEFSG are shown in Table 1.

3 | 2-D Electromagnetic Analysis

In this section, the electromagnetic performance of the DEFSG is studied using 2-D FEA. The electromagnetic performance can be classified into two stages: no-load and on-load conditions. It is important to note that to analyse the thermal behaviour of the machine, first, electromagnetic performance should be conducted to calculate losses that act as heat sources. As mentioned in Figure 2, the electromagnetic performance is analysed in two stages. First, the proposed generator has been analysed using the ambient properties for winding and PMs to reach the operating data; then, by replacing the new data, the generator is analysed once more to have precise thermal modelling.

TABLE 1 | Main design parameters.

Parameter	Value	Unit
Phase number	3	—
Stator slot number	24	—
Rotor pole pair number	10	—
Turns per coil	200	—
Rotor outer radius	100.35	mm
Stator outer radius	85	mm
Shaft radius	45	mm
Stator length	60	mm
Rotor length	70	mm
Air-gap length	0.65	mm
Volume of NdFeB35 PMs	67.2	cm^3
Volume of ferrite PMs	51.84	cm^3
Winding resistance (cold state)	5.2	Ohm
Winding resistance (hot state)	7.8	Ohm
Phase current (RMS)	3.1	A
Rated speed	750	rpm
Efficiency	0.871	—
Rated power	2300	W

3.1 | No-Load Specification

In this part, the no-load characteristics of the DEFSG are illustrated including air-gap field, back-EMF and its harmonics, and cogging torque. One way to assess the accuracy of the design is by examining the no-load characteristics. It is clear that in this part, the DEFSG is only excited by PMs, and the winding is opened. The flux density at no-load conditions is demonstrated in Figure 7. Figure 7a, shows the no-load flux distribution in the stator core and rotor segments. Also, in Figure 7b the maximum value of the air-gap flux density is about 1.64 T. As shown in Equations (10) and (12), the maximum value plays a critical part in back-EMF and output power. Moreover, the no-load back-EMF waveforms are plotted in Figure 8a. It can be seen that the peak value of the open-circuit voltage is about 403 V (FEA), whereas the measured value in the lab is around 387 V, indicating a 4% error. In addition, the harmonics spectrum of the open-circuit back-EMF measured in the lab is presented in Figure 8b. It is noticeable that in the DEFSG only odd harmonics can influence the fundamental voltage waveform. Also, the total harmonic distortion (THD) for this voltage waveshape is approximately 5%. Cogging torque is an undesirable torque undulation at no-load conditions and low speeds, resulting from force interactions between PMs and salient teeth [28]. This adverse torque creates vibrations and acoustic noise and also reduces the useful life of the machine's components [29]. The cogging torque can be determined as follows [30]:

$$T_{cogg} = \frac{\partial W}{\partial \theta} \tag{14}$$

where W and θ are the no-load magnetic energy and mechanical angle of the rotor, respectively. Equation (14) can be rewritten as follows [31]:

$$T_{cogg} = -\frac{1}{2}\phi_g^2 \frac{d\Re}{d\theta} \tag{15}$$

Where ϕ_g and $\Re$ are the air-gap flux and reluctance, respectively. One method to lower the cogging torque is to utilise an overhang rotor instead of a standard one. Hence, the prototyped DEFSG has been manufactured with this consideration in mind, so the rotor length is 70 mm up to the end-windings while the stator length is 60 mm. Since 2-D FEA is not able to differentiate the depth of each machine's components, 3-D FEA is used to illustrate the effect of the overhang rotor on cogging torque. In Figure 9, the overhang structure is shown. In Figure 10, the cogging torque waveshapes are presented. As can be seen,

17518679, 2025, 1, Downloaded from https://ietresearch.onlinelibrary.wiley.com/doi/10.1049/elp2.70042 by Fabrizio Marignetti - Cochraneltalia , Wiley Online Library on [23/01/2026]. See the Terms and Conditions (https://onlinelibrary.wiley.com/terms-and-conditions) on Wiley Online Library for rules of use; OA articles are governed by the applicable Creative Commons License

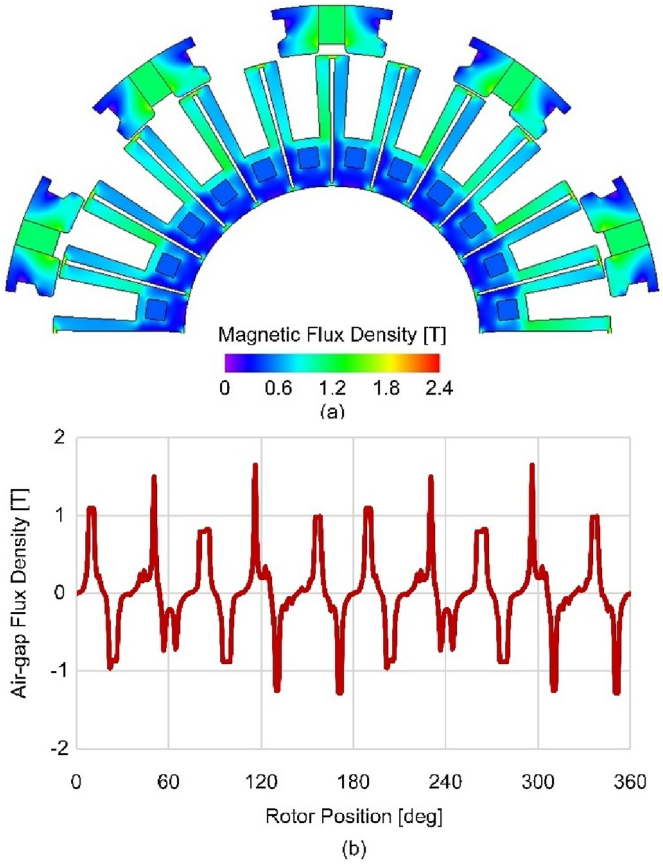

FIGURE 7 | Average no-load magnetic flux density: (a) stator core and rotor segments and (b) air gap at rated speed.

before using an overhang rotor, the peak cogging torque value was about 0.52 N.m., while this value after using an overhang rotor decreased to 0.45 N.m., which indicates a 13.46% reduction.

3.2 | On-Load Specification for Loss Calculation

In order to calculate the machine's total loss, including iron loss, PM loss and winding loss in hot state conditions serving as heat sources, the electromagnetic performance of the DEFSG should be analysed in full-load terms. The analysis comprises flux and loss distributions, full-load voltage and rated torque. The flux density at full-load conditions is demonstrated in Figure 11. It is apparent in Figure 11a, that the maximum flux density is concentrated in the stator teeth (~2.3 T) illustrates the air-gap flux density and its peak value is about 1.97 T. Furthermore, Figure 11b illustrates the air-gap flux density and its peak value is about 1.97 T. It is important to note that there is no magnetic saturation in this machine due to the magnetic properties of the rotor and stator laminations. Furthermore, 2-D FEA is employed to compute the iron loss in the DEFSG. The iron loss consists of eddy current and hysteresis loss. Although both eddy current and hysteresis loss arise from a time-varying magnetic field, hysteresis loss occurs only in ferromagnetic parts, whereas eddy current loss happens in all metallic parts [32]. Consequently, to reduce the eddy current loss, the DEFSG is constructed using thin steel laminations (0.5 mm). Furthermore, the loss density distribution of different components of DEFSG is presented in Figure 12. As shown in Figure 12a, the stator teeth have higher loss density compared to the stator yoke. Since ferrite PMs have high electrical resistance, the stator PMs' loss is not considered in this part. Figure 12b,c, illustrates the loss density in rotor segments and PMs. It is evident that the maximum rotor PMs' losses have occurred in front of the air-gap side. Since the varying magnetic flux passes through rotor segments and leaks into the cover, it induces voltages that create an eddy current in the cover. Hence, the loss density in the aluminium cover is shown in Figure 12d. In addition, the precise value of each loss is demonstrated in Table 2. The rated torque of the DEFSG is illustrated in Figure 13. In Figure 13a, the average measured torque from FEA is approximately −33.6 N.m., whereas the corresponding value obtained in the lab is around −31 N.m. as shown in Figure 13b. This results in an error of about 8%. Additionally, the torque ripple is approximately 12%. Figure 14a shows the full-load phase voltage of the proposed generator. The highest measured voltage value in the lab is about 335 V, while the FEA indicates 351 V, resulting in a 4.7% error. Moreover, the harmonics spectrum of the full-load voltage, measured in the lab, is presented in Figure 14b. Therefore, THD for the full-load voltage is about 2.34%.

4 | 3-D Thermal Analysis

To comprehend the thermal behaviour of electrical machines, it is essential to introduce thermal specifications. Such specifications encompass heat transfer coefficients, thermal resistances, heat capacitances and heat sources. In the preceding section,

17518679, 2025, 1, Downloaded from https://ietresearch.onlinelibrary.wiley.com/doi/10.1049/elp2.70042 by Fabrizio Marignetti - Cochraneltalia , Wiley Online Library on [23/01/2026]. See the Terms and Conditions (https://onlinelibrary.wiley.com/terms-and-conditions) on Wiley Online Library for rules of use; OA articles are governed by the applicable Creative Commons License

heat sources were calculated using 2-D FEA. However, the determination of other characteristics requires the use of mathematical equations. Heat transfer can be defined as energy exchange between matters due to temperature variances and can be classified into three categories: radiation, convection and conduction. Radiation occurs when heat shifts from one object (higher temperature) to another (lower temperature) without direct contact.

It is noteworthy that in the proposed generator, the radiation heat transfer is minimal and can be disregarded. Convection refers to the heat transfer process due to the movement of a fluid across a surface. This movement can be either natural or forced. The equations for convection heat transfer coefficients for rotating discs, such as the caps with ambient air and rotating cylinders, like the cover with ambient air, are comprehensively defined in ref. [33]. Conduction can be defined as heat transfer within an object or among objects in direct contact. An example

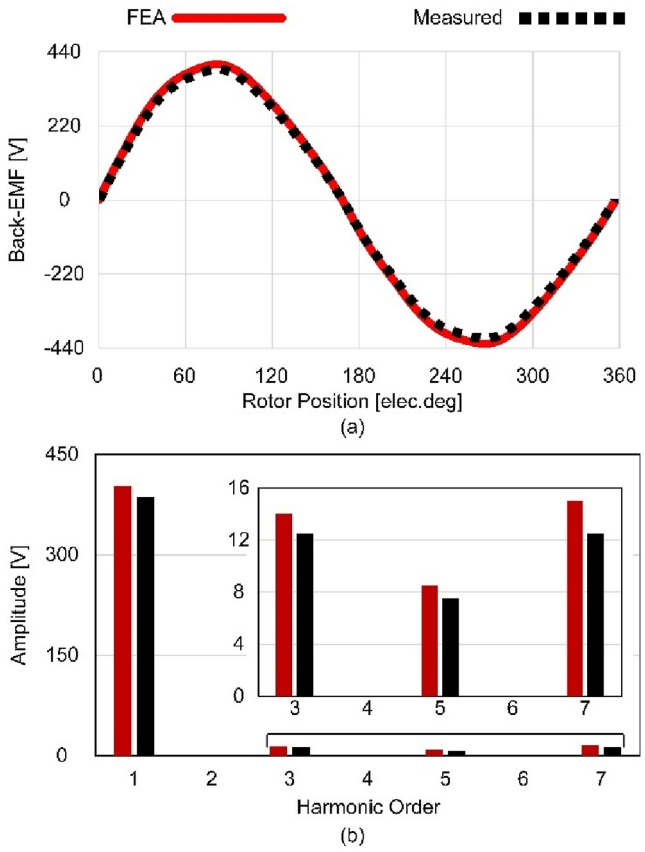

FIGURE 8 | (a) No-load back-EMF waveshapes and (b) harmonic spectrum of no-load back-EMF.

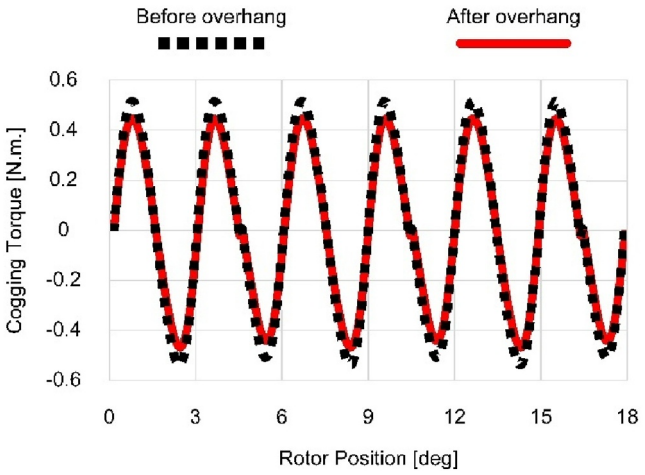

FIGURE 10 | Cogging torque waveforms.

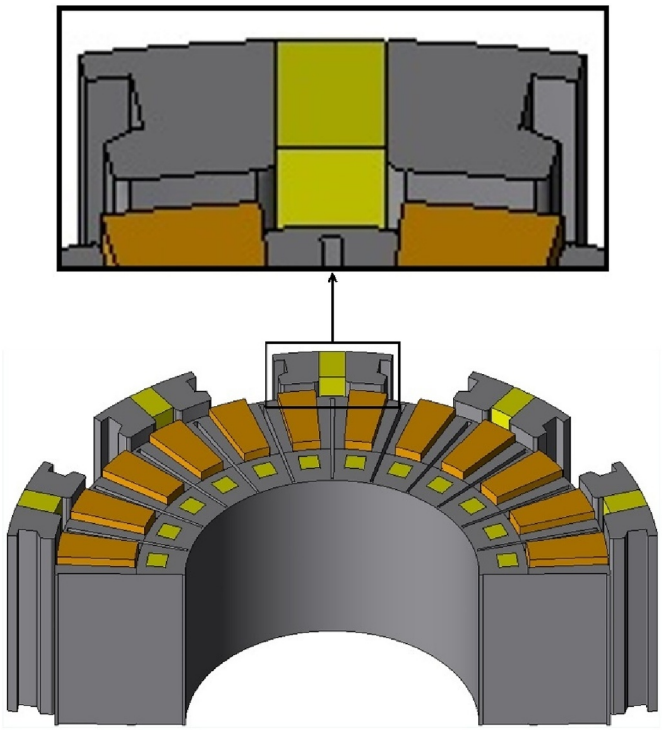

FIGURE 9 | Side view of the 3-D model of the proposed generator.

17518679, 2025, 1, Downloaded from https://ietresearch.onlinelibrary.wiley.com/doi/10.1049/elp2.70042 by Fabrizio Marignetti - Cochraneltalia , Wiley Online Library on [23/01/2026]. See the Terms and Conditions (https://onlinelibrary.wiley.com/terms-and-conditions) on Wiley Online Library for rules of use; OA articles are governed by the applicable Creative Commons License

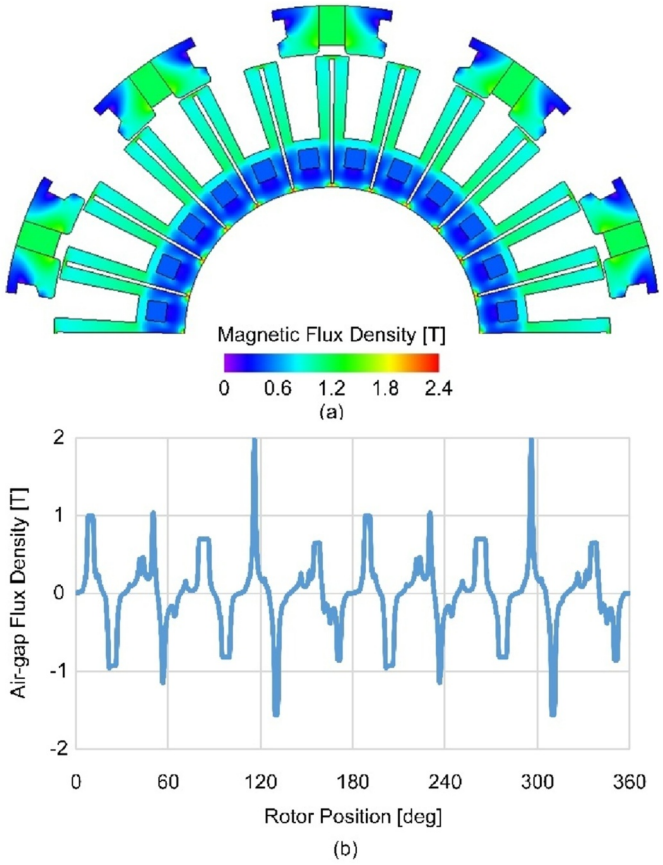

FIGURE 11 | Average full-load magnetic flux density: (a) stator core and rotor segments and (b) air gap at rated speed.

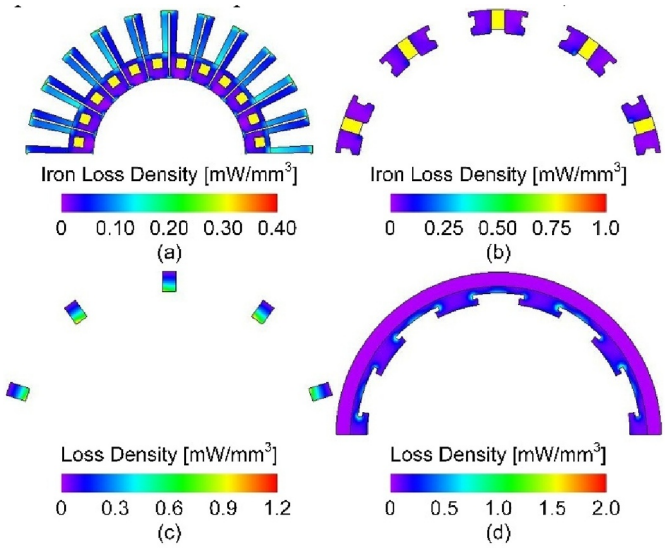

FIGURE 12 | Loss density: (a) stator, (b) rotor segments, (c) NdFeB PMs and (d) cover at full load.

TABLE 2 | Average loss at various elements of the DEFSG.

Element	Stator	Rotor	PMs	Cover	Winding
Loss (W)	32.85	5.69	15.98	40.84	203.22

of this type of heat exchange can be observed between the shaft and the stator in the DEFSG. The conduction heat transfer coefficient can be defined as follows:

$$\lambda_i = \frac{1}{\rho L_i} \tag{16}$$

where ρ is the thermal resistivity of the matter (m.°C/W), and L_i is the length of the heat path (m). Furthermore, the thermal conduction resistance can be expressed as follows [34]:

17518679, 2025, 1, Downloaded from https://ietresearch.onlinelibrary.wiley.com/doi/10.1049/elp2.70042 by Fabrizio Marignetti - Cochraneltalia , Wiley Online Library on [23/01/2026]. See the Terms and Conditions (https://onlinelibrary.wiley.com/terms-and-conditions) on Wiley Online Library for rules of use; OA articles are governed by the applicable Creative Commons License

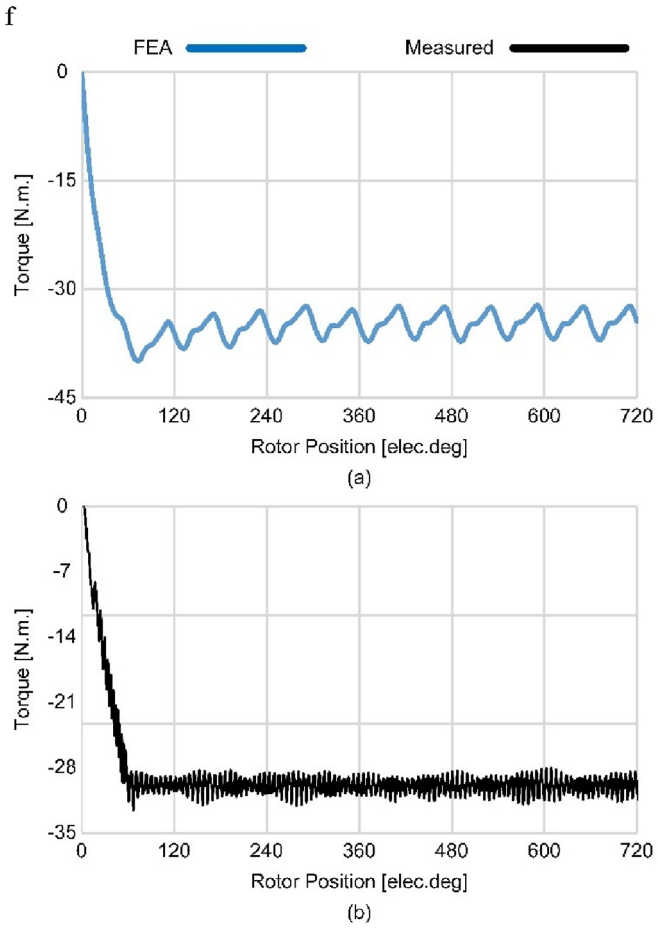

FIGURE 13 | Electromagnetic torque at full load: (a) FEA and (b) measured.

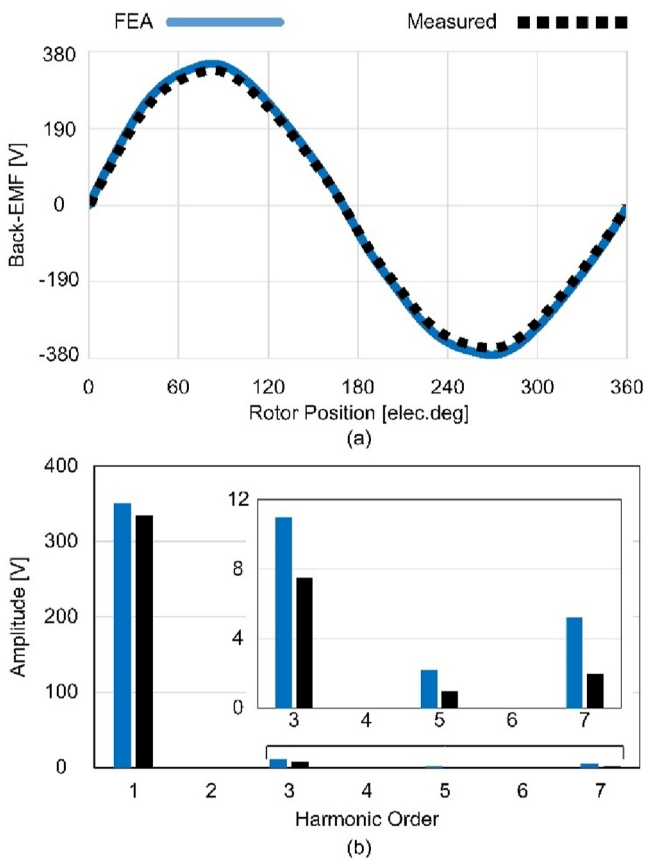

FIGURE 14 | (a) Full-load terminal voltage waveshapes and (b) harmonics spectrum of the full-load terminal voltage.

$$R_i = \frac{1}{\lambda_i A_i} \tag{17}$$

Where A_i is the cross section area of the heat path (m^2), respectively. Moreover, the convection heat transfer coefficient varies depending on the shape of the element. For instance, the equation for rotating discs differs from that for rotating cylinders. Additionally, calculating this coefficient for stationary elements, such as the stator core, can be challenging. As a result, it is typically estimated to be between 5 and 25 $(W/m^2.°C)$ for these stationary components [21]. The convection heat transfer coefficient for rotating discs such as caps can be calculated as follows:

$$\lambda_j = \frac{\overline{N_{ud}}}{\rho_{air} R_d} \tag{18}$$

Where ρ_{air} and R_d are the thermal resistivity of the air and the radius of the discs (m), respectively. Also, $\overline{N_{ud}}$ is the average Nusselt number for the rotating disc. Furthermore, the convection heat transfer coefficient for rotating cylinders such as the cover can be calculated as follows:

$$\lambda_j = \frac{\overline{N_{uc}}}{\rho_{air} D_o} \tag{19}$$

Where D_o is the outer diameter of the cylinder (m) and $\overline{N_{uc}}$ is the average Nusselt number for the rotating cylinders. It is noteworthy that the Nusselt number equations have been thoroughly defined in refs. [21, 33, 35]. In addition, the thermal convection resistance can be defined as follows [34]:

$$R_j = \frac{1}{\lambda_j A_j} \tag{20}$$

Where A_j is the cross-section area of the heat path (m^2). Finally, the heat capacitance equation can be written as follows:

$$C = mC_p \tag{21}$$

Where m and C_P are the mass of the matter (kg) and specific heat of the matter $(J/K.kg)$, respectively. Plotting a thermal circuit for the DEFSG is critical for understanding the thermal behaviour of different components. Hence, Figure 15 illustrates the thermal circuit of the DEFSG, with the rotating parts shown in green blocks and the nonrotating parts in orange. The figure also labels the copper loss, stator yoke loss, stator teeth loss, rotor segments loss, rotor PMs loss and cover loss, as Pc, Pi_1, Pi_2, Pi_3, Pe_1 and Pe_2, respectively. It is noted that the stator PMs' loss is minor and can be ignored. These losses, which perform as heat sources, were calculated in the previous part using 2-D FEA. Also, the heat transfer coefficients are denoted by the symbol λ, where λ_{12} and λ_{13} are conduction factors, while the rest of them are convection factors. In terms of heat resistance,

17518679, 2025, 1, Downloaded from https://ietresearch.onlinelibrary.wiley.com/doi/10.1049/elp2.70042 by Fabrizio Marignetti - Cochraneltalia , Wiley Online Library on [23/01/2026]. See the Terms and Conditions (https://onlinelibrary.wiley.com/terms-and-conditions) on Wiley Online Library for rules of use; OA articles are governed by the applicable Creative Commons License

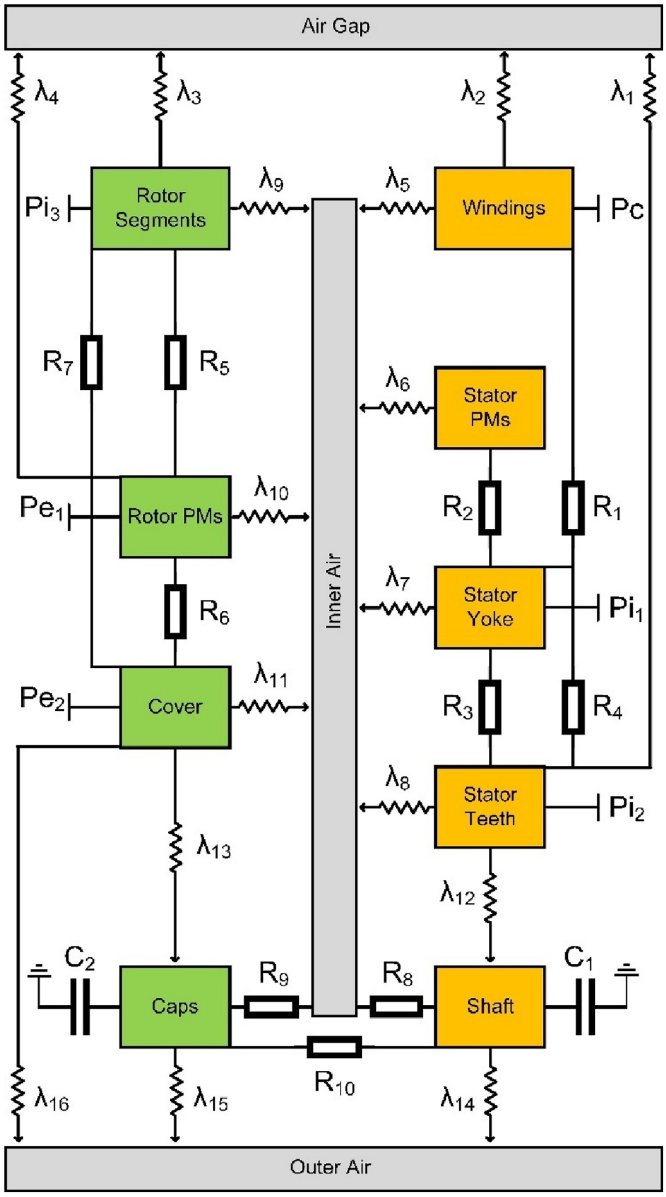

FIGURE 15 | Thermal circuit of the proposed generator.

R_1, R_2, R_3 and R_4 are the conduction heat resistors in the stator, and R_5, R_6 and R_7 are the conduction heat resistors in the rotor. Moreover, to gain a more accurate thermal analysis by 3-D FEA, it is necessary to consider nonmodelled parts such as the caps and the shaft. Therefore, R_8 and R_9 are the convection heat resistors for the nonmodelled components, and R_{10} is a conduction resistor for the mentioned components. Finally, the heat capacitances for the nonmodelled components are referred to as C_1 and C_2. The thermal characteristics of the DEFSG are listed in Table 3. Also, the thermal properties of the generator are summarised in Table 4.

4.1 | Steady-State Thermal Analysis

In this section, the thermal behaviour of the DEFSG is assessed utilising 3-D FEA. Similar to the electromagnetic analysis, the steady-state thermal analysis includes two steps. As depicted in the flowchart in Figure 2, this analysis is initially carried out under cold state conditions. Subsequently, to achieve a more precise thermal model, the analysis is repeated under hot state conditions by replacing the new data. Notably, the following findings are in operating mode (hot state). The 3-D steady-state thermal distribution of different components of the generator is shown in Figure 16. The rotor segments and NdFeB PMs are illustrated in Figure 16a, and it is evident that the inner parts in front of the air gap have a higher temperature than the other parts. Figure 16b depicts the stator core, highlighting that the stator teeth are in a hotter state than the stator yoke.

Also, the same phenomenon exists for the stator teeth-tips compared to the end parts of the teeth. Subsequently, Figure 16c, demonstrates the temperature distribution in the cover, indicating that the edges in direct contact with the rotor segments are hotter than the rest of the cover. Finally, in Figure 16d, the thermal behaviour of the coil is shown. Since the

17518679, 2025, 1, Downloaded from https://ietresearch.onlinelibrary.wiley.com/doi/10.1049/elp2.70042 by Fabrizio Marignetti - Cochraneltalia , Wiley Online Library on [23/01/2026]. See the Terms and Conditions (https://onlinelibrary.wiley.com/terms-and-conditions) on Wiley Online Library for rules of use; OA articles are governed by the applicable Creative Commons License

TABLE 3 | Thermal characteristics of the DEFSG.

Characteristics	Symbol	Definition	Value
Heat capacitances [J/°C]	C_1	Shaft	3226
	C_2	Caps	3830
Thermal resistances [°C/W]	R_1	Winding to stator yoke	0.021
	R_2	Stator PMs to stator yoke	0.054
	R_3	Stator yoke to stator teeth	0.005
	R_4	Winding to stator teeth	0.012
	R_5	Rotor segments to rotor PMs	0.022
	R_6	Rotor PMs to cover	0.066
	R_7	Rotor segments to cover	0.01
	R_8	Shaft to inner air	1.32
	R_9	Caps to inner air	0.86
	R_{10}	Shaft to caps	0.024
Heat transfer coefficients [W/m^2.°C]	λ_1 to λ_4	Stator teeth, winding, rotor segments and PMs to air gap	127.2
	λ_5	Winding to inner air	18.62
	λ_6	Stator PMs to inner air	15.87
	λ_7	Stator yoke to inner air	18.65
	λ_8	Stator teeth to inner air	13.72
	λ_9	Rotor segments to inner air	22.88
	λ_{10}	Rotor PMs to inner air	20.32
	λ_{11}	Cover to inner air	52.84
	λ_{12}	Stator core to shaft	376.7
	λ_{13}	Cover to caps	345.9
	λ_{14}	Shaft to outer air	32.2
	λ_{15}	Caps to outer air	29.06
	λ_{16}	Cover to outer air	54.87

TABLE 4 | Thermal properties of the DEFSG.

Material [20°C]	Density [kg/m^3]	Specific heat [J/kg.°C]	Thermal resistance [m.°C/W]
Air	1.204	1007	39.777
Aluminium	2698	900	0.0048
Copper	8930	385	0.0025
Steel M600	7750	460	0.0303
Steel 316	7980	502	0.0617
Neodymium N35	7500	460	0.1316
Ferrite AC-8	4900	810	0.2222

end-winding cannot be represented in 2-D FEA, and the electromagnetic and thermal analysis are coupled together, the coil is shown in a rectangular cube shape. To account for the end-winding effect, the lengths of the winding with and without the end-winding are calculated. Given the direct relationship between electrical resistance and the length of the coil, the electrical resistance values for both configurations can be determined.

The ratio of these resistances serves as a correction factor, which is then applied to the heat sources in JMAG software to adequately incorporate the impact of the end-winding. It is worth noting that the correction factor is about 1.14, also the copper loss represented in this paper has been adjusted by this factor. Furthermore, the centre of the coil appears to be cooler than its edges. In summary, the coils represent the hottest spot, while the cover is the coolest area in the operating mode. Moreover, for the initial analysis, an ambient temperature of 20°C is assumed, yielding a cold-state winding resistance of approximately 5.2 Ω. This initial assessment is performed using JMAG software, which implements the following equation for its calculations:

17518679, 2025, 1, Downloaded from https://ietresearch.onlinelibrary.wiley.com/doi/10.1049/elp2.70042 by Fabrizio Marignetti - Cochraneltalia , Wiley Online Library on [23/01/2026]. See the Terms and Conditions (https://onlinelibrary.wiley.com/terms-and-conditions) on Wiley Online Library for rules of use; OA articles are governed by the applicable Creative Commons License

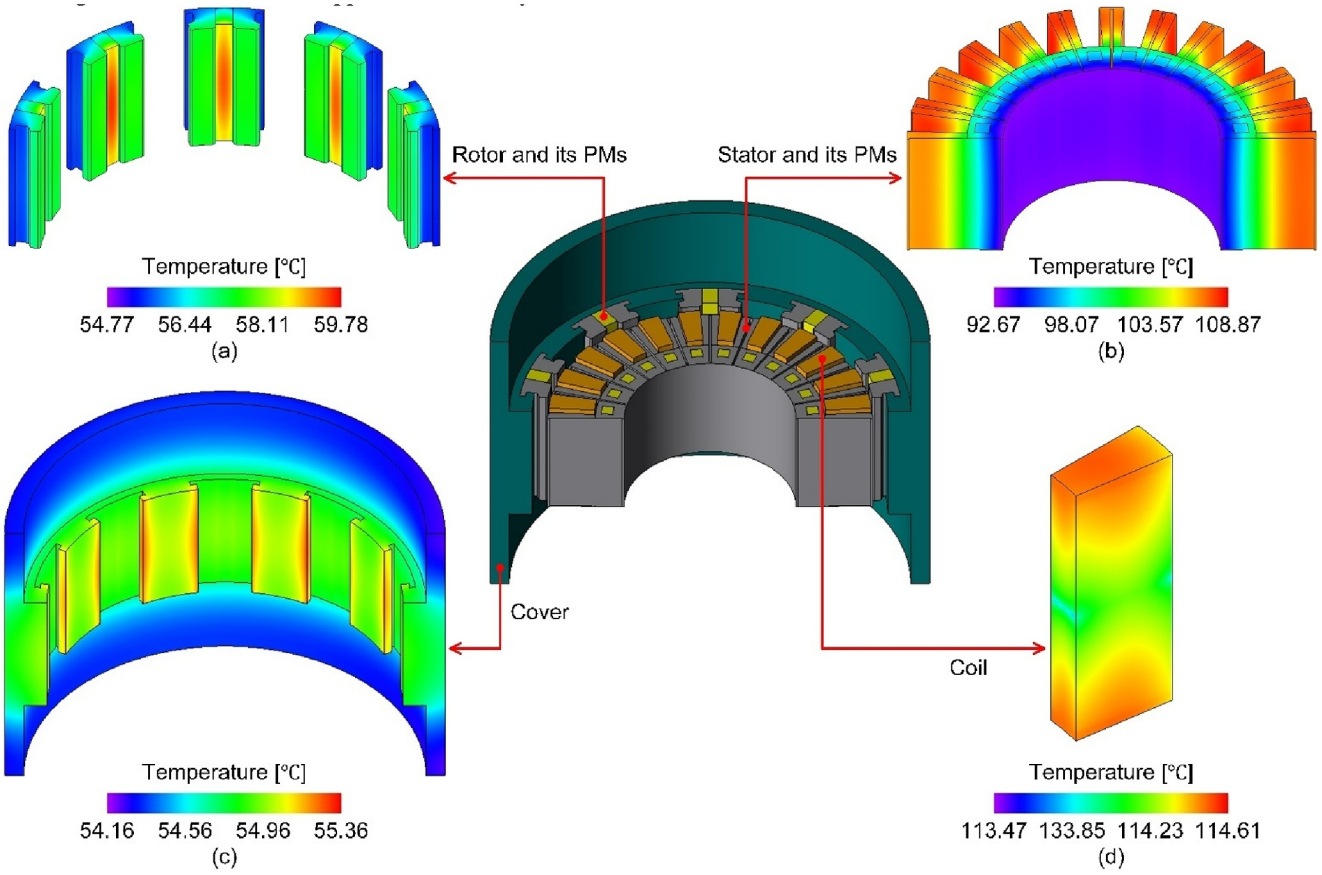

FIGURE 16 | Temperature distribution in the DEFSG: (a) rotor segments and NdFeB PMs, (b) stator core and ferrite PMs, (c) cover and (d) winding.

$$R_{\text{hot}} = R_{\text{ref}}\left(\frac{C_F + T_{\text{hot}}}{C_F + T_{\text{ref}}}\right) \tag{22}$$

Where R_{hot} and R_{ref} are the corrected and reference resistances, respectively. Also, T_{hot} and T_{ref} are the corrected and reference temperature of the winding (°C), and C_F is the correction factor for copper (~234.5). Upon completion of the first analysis, the winding temperature is observed to reach nearly 105°C, resulting in a winding resistance of approximately 6.94 Ω. In the second analytical stage, the reference temperature and resistance are adjusted to 105°C and 6.94 Ω, respectively. Following this analysis, the winding resistance is found to increase to approximately 7.13 Ω, while the temperature of the coils escalates to 114.5°C, which will be discussed in Section 4. Furthermore, the same procedure is implemented for the PMs. Initially, the reference temperature for the PMs is established at 20°C, after which an analysis is conducted. It is observed that the temperature of the ferrite magnet reaches approximately 96.5°C, while the temperature of the neodymium magnet rises to around 56°C. Subsequently, the reference temperatures of the magnets will be adjusted to these measured values, and the analysis will be performed again. The rationale for this procedure lies in the fact that, by aligning the reference temperature with the actual operating conditions, the software will automatically modify the B-H curve of the magnets. This adjustment results in a more precise determination of the operating point for the magnets, thereby enhancing the reliability of the output data.

It is noteworthy that the following results are in operating mode (hot state).

4.2 | Transient-State Thermal Analysis

In Figure 17, the temperature profile of various elements of the generator is presented. It is clear that the simulation duration is 300 min, with the initial temperature set to the ambient level. The thermal behaviour of nonrotating parts is visualised in Figure 17a, while the same graph for rotating parts is in Figure 17b. As indicated in Figure 17, the coil temperature has increased to almost 114°C, establishing it as the hottest spot in the generator. In terms of permanent magnets, the ferrite PM temperature went up to ~95°C, while the neodymium PM temperature rose to ~58°C. That is the reason behind the placement of ferrite PMs in the stator yoke and neodymium PMs in the rotor since the operating temperature of ferrite PMs is high, while the neodymium PMs are prone to demagnetisation in high-temperature conditions. It is evident that the nonrotating elements are approximately twice as hot as the rotating elements. Also, the exact temperature value of each element is shown in Table 5.

5 | Comparison of Basic and Proposed Topologies

This section compares the electromagnetic performance and thermal behaviour of the basic topology with the proposed

17518679, 2025, 1, Downloaded from https://ietresearch.onlinelibrary.wiley.com/doi/10.1049/elp2.70042 by Fabrizio Marignetti - Cochraneltalia , Wiley Online Library on [23/01/2026]. See the Terms and Conditions (https://onlinelibrary.wiley.com/terms-and-conditions) on Wiley Online Library for rules of use; OA articles are governed by the applicable Creative Commons License

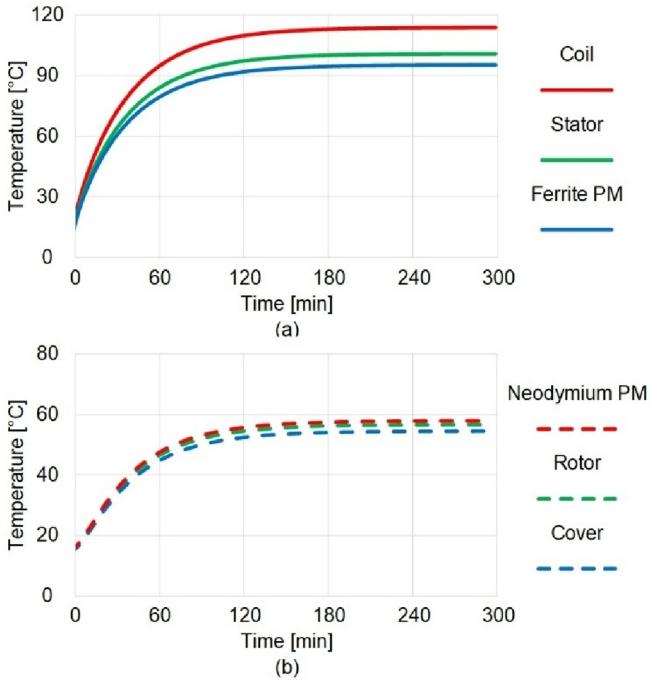

FIGURE 17 | Transient temperature graph of different generator's elements: (a) nonrotating elements and (b) rotating elements.

TABLE 5 | Temperature of different elements of the DEFSG.

Element	Temperature [°C]
Coil	113.98
Stator	101.02
Ferrite PM	95.41
NdFeB PM	57.84
Rotor	56.69
Cover	54.63

topology. As shown in Figure 18, the rotor segments and the cover are identical for both topologies; however, the stator core is where the key difference lies. The basic topology employs a simple structure for the stator core, whereas the proposed topology (DEFSG) incorporates ferrite magnets in the stator core along with flux barriers, as previously mentioned. The use of flux barriers is intended to improve thermal management and to separate the positive and negative cycles of flux linkage between the stator teeth and the rotor segments. Furthermore, it is evident that the utilisation of ferrite magnets enhances the power density of the machine. The electromagnetic characteristics of both topologies are summarised in Table 6. It is evident that the output power of the DEFSG is approximately 2.5% higher than that of the basic topology, which can be attributed to its use of ferrite magnets. Additionally, the proposed topology shows improved performance in terms of THD and back-EMF values. Moreover, the thermal characteristics of the stator core for both configurations are depicted in Figure 19. As shown in Figure 19a, the maximum temperature of the stator core is observed in the stator teeth, reaching approximately 115.5°C for the basic topology. In comparison, the proposed topology exhibits a maximum temperature of around 108.5°C, demonstrating that the stator core of the DEFSG operates at a temperature that is 7°C lower than that of the basic configuration. This enhanced thermal performance can be attributed to the incorporation of flux barriers within the stator core, which significantly improves the thermal management of the machine.

6 | Experimental Validation

After conducting an analysis of the electromagnetic-thermal performance of the generator using 2-D and 3-D FEA, it is essential to evaluate the performance of the prototyped generator in the lab. The electromagnetic experimental performance was displayed in Section 3, and in this section, the focus is on the thermal experimental test of DEFSG. Hence, as shown in Figure 20, two thermal sensors were fixed in the stator to compute the temperatures of the hottest spots in DEFSG. The pale blue circle indicates the position of the thermal sensor in the stator tooth-tip and the orange one denotes the location of the thermal sensor between the coils. Moreover, a laser thermometer was employed to gauge the temperature of the cover at the specific location shown by the green circle. Subsequently, Figure 21 illustrates the test bench of the proposed generator. It is apparent that the prototyped generator was coupled to an induction motor which acts as the generator's mover through a torque transducer. Also, an inverter and a tachometer were employed to control and check the mover's speed. Furthermore, the generator was linked to a three-phase resistive load with a star connection. The experimental test lasted 5 h under rated load conditions at ambient temperature. The temperatures of the case study spots were recorded every minute. Furthermore, the waveforms including transient temperature, no-load voltage, on-load voltage, cogging torque and rated torque, which have been calculated in the lab, are recorded by the data acquisition system (DAS). Figure 22, indicates the comparison between the measured lab temperatures and temperature results by 3-D FEA. It is evident that after ~3 h, the generator's thermal behaviour stabilises, reaching a steady-state mode The coil and stator tooth-tip measured temperatures by thermal sensors are displayed in Figure 22a,b. In the steady-state mode, the measured temperature of the coils reaches 122.6°C, while the FEA reported result is ~114°C, showing an error of about 8.5°C. Moreover, the maximum measured temperature of the stator tooth-tip is approximately 118°C, while the FEA registered temperature is ~107°C, indicating a temperature difference of around 10°C. Additionally, the temperature of the rotating cover measured by a laser thermometer is depicted in Figure 22c. The peak temperature value of the cover in the lab is ~60°C, while the FEA value is around 55°C, resulting in a difference of 5°C. Furthermore, the highest recorded temperatures of the case study points in the lab and by 3-D FEA are listed in Table 7. The results obtained from Figure 22 and Table 7 demonstrate a strong agreement between the laboratory calculations and the 3-D FEA. This indicates that this approach is an effective technique that not only reduces computational time but also enhances calculation precision.

17518679, 2025, 1, Downloaded from https://ietresearch.onlinelibrary.wiley.com/doi/10.1049/elp2.70042 by Fabrizio Marignetti - Cochraneltalia , Wiley Online Library on [23/01/2026]. See the Terms and Conditions (https://onlinelibrary.wiley.com/terms-and-conditions) on Wiley Online Library for rules of use; OA articles are governed by the applicable Creative Commons License

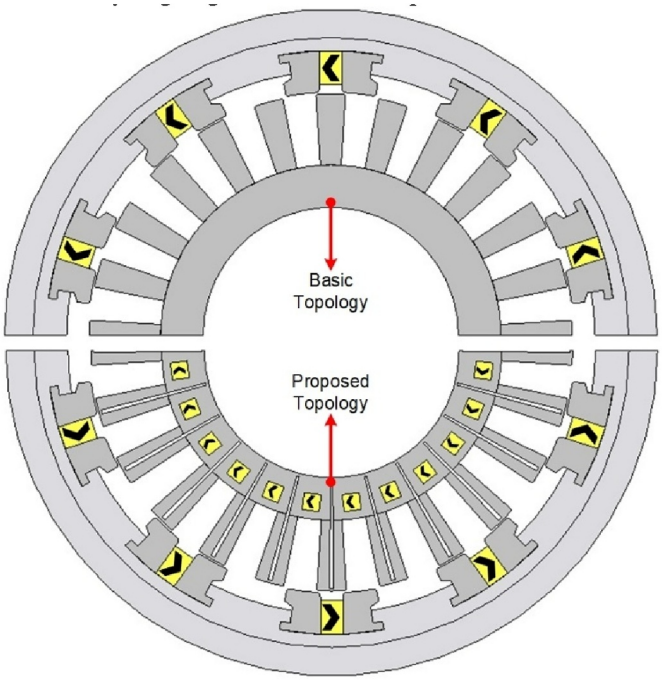

FIGURE 18 | Configurations of basic and proposed topologies.

TABLE 6 | Electromagnetic characteristics of the basic topology and DEFSG.

Parameter	Basic topology	Proposed topology
Power (W)	2243	2300
Back-EMF (V)	281.4	285
THD (%)	6.5	5
Rated torque (N.m)	−32.8	−33.6

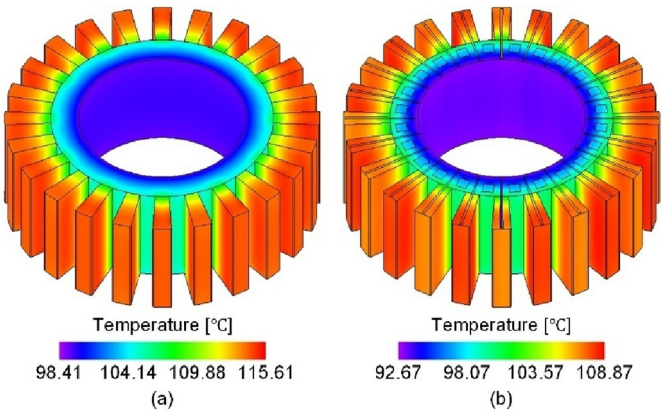

FIGURE 19 | Thermal distribution in the stator core for: (a) basic topology and (b) proposed topology.

7 | Conclusion

This paper introduced a new outer rotor dual-PM excited flux-switching generator with an overhang structure for wind turbine applications. The proposed generator utilised ferrite PMs in the stator yoke and neodymium PMs in the rotor segments. In this study, a 2-D FEA electromagnetic analysis coupled with a 3-D FEA thermal analysis reached an accurate and fast method based on the comparison between the simulation results and the experimental data. It is noteworthy that the simulation duration for 2-D FEA electromagnetic analysis coupled with 3-D FEA steady-state thermal analysis was about 1 hour. Also, the transient-state thermal analysis took about 6 h. This notable efficiency underscores the classification of this method as a rapid analytical approach. In terms of electromagnetic behaviour, the generator demonstrated strong electromagnetic performance, with a no-load voltage THD of less than 5% and a full-load voltage THD of less than 2.5%. Also, the overhang rotor

17518679, 2025, 1, Downloaded from https://ietresearch.onlinelibrary.wiley.com/doi/10.1049/elp2.70042 by Fabrizio Marignetti - Cochraneltalia , Wiley Online Library on [23/01/2026]. See the Terms and Conditions (https://onlinelibrary.wiley.com/terms-and-conditions) on Wiley Online Library for rules of use; OA articles are governed by the applicable Creative Commons License

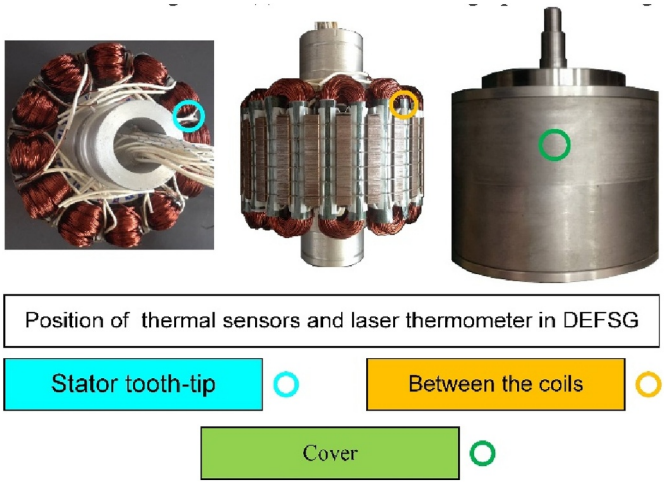

FIGURE 20 | Location of different sensors in the DEFSG.

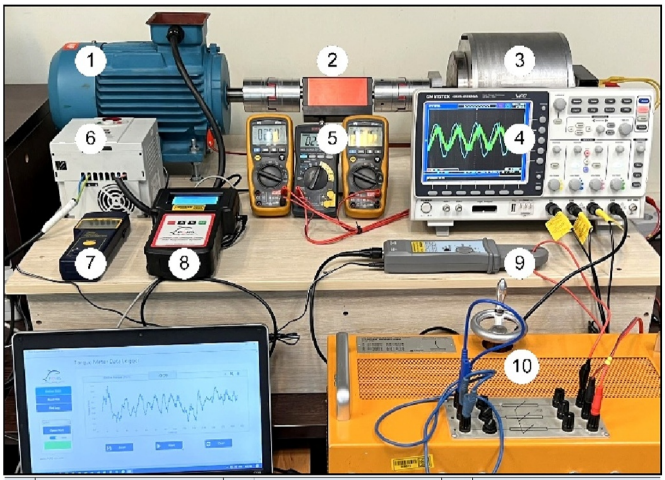

1	Induction Motor	2	Transducer	3	DEFSG
4	Oscilloscope	5	Thermometers	6	Inverter
7	Tachometer	8	Data System	9	Current Probe
		10	Resistive Load		

FIGURE 21 | Experimental test validation of the prototyped generator.

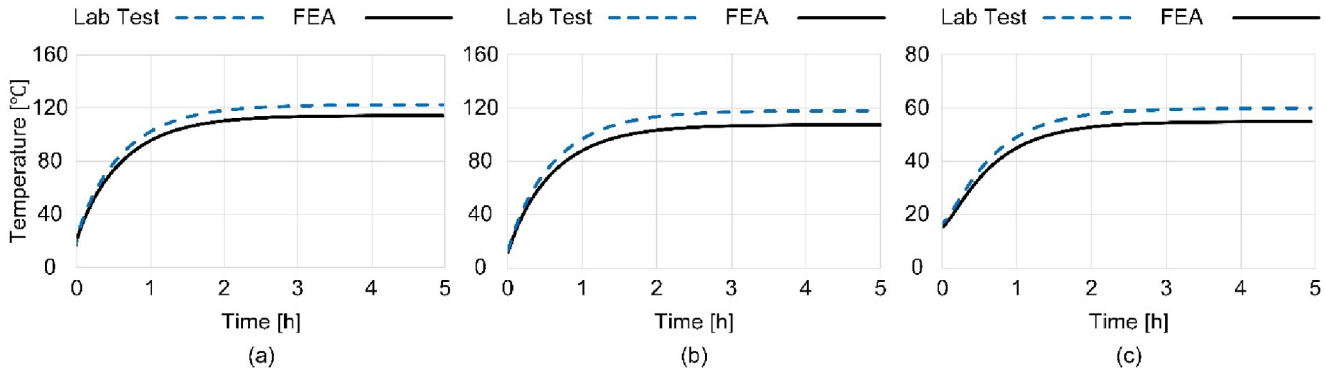

FIGURE 22 | The measured lab temperature compared to the 3-D FEA transient results: (a) coils, (b) stator tooth-tip and (c) cover.

contributed to a reduction in cogging torque of almost 13.5%. Moreover, the 2-D magnetic flux density of the generator did not exhibit any signs of magnetic saturation. The recorded rated torque was around 31 N.m. at 750 rpm, making it an excellent candidate for direct-drive wind turbines due to its compact dimensions. In terms of the thermal behaviour, a precise thermal

17518679, 2025, 1, Downloaded from https://ietresearch.onlinelibrary.wiley.com/doi/10.1049/elp2.70042 by Fabrizio Marignetti - Cochraneltalia , Wiley Online Library on [23/01/2026]. See the Terms and Conditions (https://onlinelibrary.wiley.com/terms-and-conditions) on Wiley Online Library for rules of use; OA articles are governed by the applicable Creative Commons License

TABLE 7 | The measured temperature of various elements in the lab and FEA.

Element	Temperature in the lab [°C]	Temperature FEA [°C]	Temperature difference [°C]
Coils	122.60	114.05	8.55
Stator tooth-tip	117.80	107.11	10.69
Cover	59.70	54.71	4.99

circuit of the generator was introduced, with each element being separately modelled in this circuit. A comprehensive thermal analysis was conducted to assess the steady-state and transient thermal performances of the key components. It revealed that the temperature of the stator is nearly double that of the rotor. This is why the neodymium PMs were placed in the rotor, as they are susceptible to demagnetisation at high temperatures. Furthermore, the temperature of each element was within an acceptable range, and there was a small deviation between the measured and the simulation temperatures, demonstrating the successful implementation of the proposed coupled method.

Author Contributions

Amir Ebrahimi Shohani: conceptualization, formal analysis, investigation, writing – original draft, writing – review and editing. **Mohammad Farahzadi:** formal analysis, investigation, validation. **Salman Ali:** funding acquisition, resources. **Karim Abbaszadeh:** project administration, supervision. **Fabrizio Marignetti:** supervision, validation. **Fariba Farrokh:** data curation, visualization.

Acknowledgements

The authors have nothing to report.

Conflicts of Interest

The authors declare no conflicts of interest.

Data Availability Statement

The data that support the findings of this study are available from the corresponding author upon reasonable request.

References

1. F. Li and X. Zhu, "Comparative Study of Stepwise Optimization and Global Optimization on a Nine-Phase Flux-Switching PM Generator," *Energies* 14, no. 16 (2021): 4754, https://doi.org/10.3390/en14164754.

2. P. Seangwong, S. Chamchuen, N. Fernando, A. Siritaratiwat, and P. Khunkitti, "A Novel Six-Phase V-Shaped Flux-Switching Permanent Magnet Generator for Wind Power Generation," *Energies* 15, no. 24 (2022): 9608, https://doi.org/10.3390/en15249608.

3. V. Torn, P. Seangwong, N. Fernando, A. Siritaratiwat, and P. Khunkitti, "Performance Improvement of Flux Switching Permanent Magnet Wind Generator Using Magnetic Flux Barrier Design," *Sustainability* 15, no. 11 (2023): 8867, https://doi.org/10.3390/su15118867.

4. F. Porté-Agel, M. Bastankhah, and S. Shamsoddin, "Wind-Turbine and Wind-Farm Flows: A Review," *Boundary-Layer Meteorology* 174, no. 1 (2020): 1–59, https://doi.org/10.1007/s10546-019-00473-0.

5. V. L. Okulov and G. A. Van Kuik, "The Betz–Joukowsky Limit: On the Contribution to Rotor Aerodynamics by the British, German and Russian Scientific Schools," *Wind Energy* 15, no. 2 (2012): 335–344, https://doi.org/10.1002/we.464.

6. S. Cai, J. L. Kirtley, and C. H. Lee, "Critical Review of Direct-Drive Electrical Machine Systems for Electric and Hybrid Electric Vehicles," *IEEE Transactions on Energy Conversion* 37, no. 4 (2022): 2657–2668, https://doi.org/10.1109/tec.2022.3197351.

7. M. Yousuf, F. Khan, A. Tameemi, W. Ullah, and S. Akbar, "Investigation of Open Circuit DC Winding Induced Voltage Reduction Techniques in Five Phase Non-Overlapped Wound Field Flux Switching Machines," *IEEE Access* 12 (2024): 45865–45878, https://doi.org/10.1109/ACCESS.2024.3382211.

8. F. Farrokh, A. Vahedi, H. Torkaman, M. Banejad, A. J. Mahdi, and M. J. Mohammed, "Demagnetization and Fault-Tolerance Analysis in Dual-Stator Axial-Field Flux-Switching Permanent Magnet Motor," *IEEE Access* 12 (2024): 102579–102591, https://doi.org/10.1109/access.2024.3431438.

9. W. Ullah, F. Khan, S. Hussain, M. Yousaf, and S. Akbar, "Analytical Modeling and Optimization of Partitioned Permanent Magnet Consequent Pole Switched Flux Machine With Flux Barrier," *IEEE Access* 10 (2022): 123905–123919, https://doi.org/10.1109/access.2022.3224020.

10. S. Rauch and L. J. Johnson, "Design Principles of Flux-Switch Alternators [Includes Discussion]," *Transactions of the American Institute of Electrical Engineers. Part III: Power Apparatus and Systems* 74, no. 3 (1955): 1261–1268, https://doi.org/10.1109/aieepas.1955.4499226.

11. E. Hoang, A. Ben Ahmed, and J. Lucidarme, "Switching Flux Permanent Magnet Polyphased Synchronous Machines," in *European Conference on Power Electronics and Applications*, Vol. 3, (1997), 3.903–3.908: Proceedings Published by Various Publishers.

12. H. Ding, W. Sixel, L. F. Handy-Cardenas, and B. Sarlioglu, "Investigation of the Self-Cooling Characteristics of a Novel Flux-Switching Permanent Magnet Machine," in *2019 IEEE Energy Conversion Congress and Exposition (ECCE)* (IEEE, 2019), 6562–6568.

13. L. Liu, S. Ding, C. Liu, D. Zhang, and Q. Wang, "Electromagnetic Performance Analysis and Thermal Research of an Outer-Rotor I-Shaped Flux-Switching Permanent-Magnet Motor With Considering Driving Cycles," *IET Electric Power Applications* 13, no. 12 (2019): 2052–2057, https://doi.org/10.1049/iet-epa.2018.5046.

14. L. Mo, T. Zhang, and Q. Lu, "Thermal Analysis of a Flux-Switching Permanent-Magnet Double-Rotor Machine With a 3-D Thermal Network Model," *IEEE Transactions on Applied Superconductivity* 29, no. 2 (2019): 1–5, https://doi.org/10.1109/tasc.2019.2892307.

15. S. Khalesidoost, J. Faiz, and E. Mazaheri-Tehrani, "An Overview of Thermal Modelling Techniques for Permanent Magnet Machines," *IET Science, Measurement & Technology* 16, no. 4 (2022): 219–241, https://doi.org/10.1049/smt2.12099.

16. W. Yu, Z. Wu, and W. Hua, "Thermal Analysis of a Flux-Switching Permanent Magnet Machine for Hybrid Electric Vehicles," *World Electric Vehicle Journal* 14, no. 5 (2023): 130, https://doi.org/10.3390/wevj14050130.

17. M. Liu, W. Sixel, B. Sarlioglu, and G. Nellis, "Influence of Winding Topologies and Encapsulation Materials on FSPM Machine Thermal Performance," *IET Electric Power Applications* 14, no. 9 (2020): 1604–1611, https://doi.org/10.1049/iet-epa.2019.1058.

18. W. Ullah, F. Khan, M. Umair, and E. Sulaiman, "Coupled Electromagnetic-Thermal Analysis of Segmented PM Consequent Pole

17518679, 2025, 1, Downloaded from https://ietresearch.onlinelibrary.wiley.com/doi/10.1049/elp2.70042 by Fabrizio Marignetti - Cochraneltalia , Wiley Online Library on [23/01/2026]. See the Terms and Conditions (https://onlinelibrary.wiley.com/terms-and-conditions) on Wiley Online Library for rules of use; OA articles are governed by the applicable Creative Commons License

Flux Switching Machine," *Chinese Journal of Electrical Engineering* 7, no. 2 (2021): 50–60, https://doi.org/10.23919/cjee.2021.000015.

19. J. Wang, Y. Hu, M. Cheng, B. Li, and B. Chen, "Bidirectional Coupling Model of Electromagnetic Field and Thermal Field Applied to the Thermal Analysis of the FSPM Machine," *Energies* 13, no. 12 (2020): 3079, https://doi.org/10.3390/en13123079.

20. A. Zarghani, M. Farahzadi, A. Ghaheri, and K. Abbaszadeh, "Accurate 3D Thermal Network Development for Direct-Drive Outer-Rotor Hybrid-PM Flux-Switching Generator," *Chinese Journal of Electrical Engineering* 10, no. 2 (2024): 80–92, https://doi.org/10.23919/cjee.2024.000059.

21. M. Farahzadi, K. Abbaszadeh, and S. Mirnikjoo, "Electromagnetic-Thermal Analysis of a Hybrid-Excited Flux Switching Permanent Magnet Generator for Wind Turbine Application," *IEEE Transactions on Energy Conversion* 38, no. 3 (2023): 1962–1973, https://doi.org/10.1109/tec.2023.3269038.

22. A. Tummala, R. K. Velamati, D. K. Sinha, V. Indraja, and V. H. Krishna, "A Review on Small Scale Wind Turbines," *Renewable and Sustainable Energy Reviews* 56 (2016): 1351–1371, https://doi.org/10.1016/j.rser.2015.12.027.

23. M. Balat, "A Review of Modern Wind Turbine Technology," *Energy Sources, Part A* 31, no. 17 (2009): 1561–1572, https://doi.org/10.1080/15567030802094045.

24. M. Farahzadi, S. Ali, S. Mirnikjoo, K. Abbaszadeh, F. Marignetti, and M. Salehi, "Design and Experimental Validation of a New Outer Rotor Double PM Excited Flux Switching Generator for Direct Drive Wind Turbines," *IEEE Access* 12 (2024): 62256–62267, https://doi.org/10.1109/access.2024.3394968.

25. R. Nasiri-Zarandi, A. Ghaheri, and K. Abbaszadeh, "Thermal Modeling and Analysis of a Novel Transverse Flux HAPM Generator for Small-Scale Wind Turbine Application," *IEEE Transactions on Energy Conversion* 35, no. 1 (2019): 445–453, https://doi.org/10.1109/tec.2019.2936683.

26. Y. Shi, L. Jian, J. Wei, Z. Shao, W. Li, and C. C. Chan, "A New Perspective on the Operating Principle of Flux-Switching Permanent-Magnet Machines," *IEEE Transactions on Industrial Electronics* 63, no. 3 (2015): 1425–1437, https://doi.org/10.1109/tie.2015.2492940.

27. A. Zohoori, A. Vahedi, M. A. Noroozi, and S. Meo, "A New Outer-Rotor Flux Switching Permanent Magnet Generator for Wind Farm Applications," *Wind Energy* 20, no. 1 (2017): 3–17, https://doi.org/10.1002/we.1986.

28. E. Brescia, M. Palmieri, P. R. Massenio, G. L. Cascella, and F. Cupertino, "Cogging Torque Suppression of Modular Permanent Magnet Machines Using a Semi-Analytical Approach and Artificial Intelligence," *IEEE Access* 11 (2023): 39405–39417, https://doi.org/10.1109/access.2023.3267159.

29. O. Ocak and M. Aydin, "An Innovative Semi-FEA Based, Variable Magnet-Step-Skew to Minimize Cogging Torque and Torque Pulsations in Permanent Magnet Synchronous Motors," *IEEE Access* 8 (2020): 210775–210783, https://doi.org/10.1109/access.2020.3038340.

30. W. Wang, H. Ma, X. Qiu, and J. Yang, "A Calculation Method for the On-Load Cogging Torque of Permanent Magnet Synchronous Machine," *IEEE Access* 7 (2019): 106316–106326, https://doi.org/10.1109/access.2019.2929429.

31. M. A. Baig, J. Ikram, A. Iftikhar, S. S. H. Bukhari, N. Khan, and J.-S. Ro, "Minimization of Cogging Torque in Axial Field Flux Switching Machine Using Arc Shaped Triangular Magnets," *IEEE Access* 8 (2020): 227193–227201, https://doi.org/10.1109/access.2020.3044922.

32. W. Ma, Y. Huang, D. Gong, W. Li, and Y. Wang, "Iron Loss Analysis and Efficiency Calculation of Double Stator HTS Machine With Stationary Seal," *IEEE Access* 10 (2022): 88956–88969, https://doi.org/10.1109/access.2022.3200742.

33. J. F. Gieras, R.-J. Wang, and M. J. Kamper, *Axial Flux Permanent Magnet Brushless Machines* (Springer Science & Business Media, 2008).

34. W. Yu, W. Hua, J. Qi, et al., "Coupled Magnetic Field-Thermal Network Analysis of Modular-Spoke-Type Permanent-Magnet Machine for Electric Motorcycle," *IEEE Transactions on Energy Conversion* 36, no. 1 (2020): 120–130, https://doi.org/10.1109/tec.2020.3006098.

35. R. Nasiri-Zarandi, M. Farahzadi, and M. S. Toulabi, "Thermal Modeling of an Outer Rotor PM Assisted SynRM for the Electric Bike Applications Using a New 3-D LPTN," *IEEE Transactions on Transportation Electrification* (2024).

17518679, 2025, 1, Downloaded from https://ietresearch.onlinelibrary.wiley.com/doi/10.1049/elp2.70042 by Fabrizio Marignetti - Cochraneltalia , Wiley Online Library on [23/01/2026]. See the Terms and Conditions (https://onlinelibrary.wiley.com/terms-and-conditions) on Wiley Online Library for rules of use; OA articles are governed by the applicable Creative Commons License